Two-dimensional Particle-in-Cell modeling of blow-off impulse by X-ray irradiation[*]

Ruibo Li,[1] Jin-Long Jiao,[2, †] Hui Luo,[1, ‡] Dezhi Zhang,[3] Dengwang Wang,[3] and Kai Wang[2, §]

[1]*Graduate School of China Academy of Engineering Physics, Beijing 100193, China*
[2]*Zhejiang Institute of Modern Physics, Institute of Astronomy,*
School of Physics, Zhejiang University, Hangzhou 310027, China
[3]*National Key Laboratory of Intense Pulsed Radiation Simulation and Effect,*
Northwest Institute of Nuclear Technology, Xi'an 710024, China

Space objects, such as spacecraft or missiles, might be exposed to intense X-rays in outer space, leading to severe damage. How to reinforce these objects to reduce damage from X-ray irradiation is a significant concern. Blow-off impulse (BOI) is a crucial physical quantity for investigating the material damage induced by X-ray irradiation. However, the accurate calculation of the BOI is a challenge, particularly for the large deformation of materials with complex configurations. In this paper, we develop a novel two-dimensional Particle-in-Cell (PIC) code, *Xablation2D*, to calculate the BOIs under far-field X-ray irradiation. This significantly reduces the dependence on grid shape for numerical simulation. The reliability of this code is verified by the simulation results from the open-source codes, and the calculated BOIs are consistent with experimental and analytical results.

Keywords: X-ray irradiation, Energy deposition, Blow-off impulse, Particle-in-Cell

I. INTRODUCTION

High energy-density X-ray irradiation induced by a nuclear explosion in outer space can damage spacecrafts or missiles [1–3]. If the X-ray source is located in the far-field, the surface material of these objects might undergo sublimation. The vaporized material rapidly expands outward, causing a blow-off impulse (BOI). The BOI loads on the remaining solid material, generating a compressive stress wave that propagates inward, which is called vapor recoil loading. On the other hand, the pressure disturbance caused by the non-uniform deposition energy as thermal stress loading generates a thermal shock wave characterized by compression at the front and tension at the rear [4]. These stress waves form a thermal shock wave, and induce mechanical damage to material structures and make space objects lose efficacy permanently. How to reinforce the space objects to reduce damage by X-ray irradiation is a valuable issue that has been investigated extensively.

The BOI, as a measurable physical quantity, plays a crucial role in investigating the material damage induced by X-ray irradiation [5–8]. Since the pulse duration of X-rays induced by a nuclear explosion and the time taken for phase transition in the material are both $\mathcal{O}(0.1\ \mu s)$, significantly shorter than the time it takes for dynamic response and stress wave propagation within the material. It is reasonable to decouple the energy deposition process from the whole X-ray irradiation. In early research, several physical analytical models were proposed to calculate the BOI under the assumption of instantaneous deposition energy [9, 10], including the Whitener model, the BBAY model, and the modified BBAY (MBBAY) model. These models have analytical formulas for the BOI,

and they are extensively utilized in subsequent simulation and experimental works [9, 11–14]. The predictive capabilities of these models are satisfactory when it comes to calculating the BOI for one-dimensional or simple configuration materials, but their accuracy falls short when applied to complex configuration materials and non-instantaneous deposition energy. The other approach for calculating the BOI is to combine the energy deposition process with the generation and propagation of stress wave, and simulate the whole X-ray irradiation. With the rapid development of computational fluid dynamics, a series of codes, referred to this approach, have been developed to calculate the BOI for multi-dimensional materials, such as *PUFF-TFT* [15], *CTH* [16], *LS-DYNA* [17], *ABAQUS* [18], *RAMA* [19–21], *TSHOCK3D* [22] and so on. These codes employ either the finite difference or finite element method, and incorporate Eulerian or Lagrangian descriptions for numerical simulation, which enables the calculation of the temporal evolution of the BOI and results in significant enhancements in computational accuracy. Nevertheless, there are certain disadvantages associated with these codes, i.e., the Eulerian description is hard to track fluid interfaces, while the Lagrangian description is prone to mesh distortion when encountering large material deformations. In addition to the mesh method mentioned above, another simulation tool is the Monte Carlo method [23, 24]. However, this method relies on statistics, has low efficiency, and requires a significant amount of computational resources.

Particle-in-Cell (PIC) is a particle-mesh method that is developed by F. H. Harlow's team for the first time when studying gas dynamics problems at the Los Alamos National Laboratory in the United States [25, 26]. Then, it is widely generalized to computational plasma physics [27]. The Harlow's PIC method discretizes the fluid into free-moving pseudo-particles in the spatial grid, and combines the Lagrangian and Eulerian descriptions, which has advantages in simulating large deformation problems in materials with complex configurations. As far as we know, there is no reports on PIC code for the BOI calculation. In this paper, we develop

a novel two-dimensional PIC code, *Xablation2D*. This code can be used to calculate the BOI produced by X-ray irradiating materials.

The paper is organized as follows. In section II, we discuss the theoretical basis and essential modeling techniques, including the fluid PIC scheme, and the three main modules of the code. In section III, we describe the algorithm implementation in detail, including initialization, discretization, and parallelization. Section IV is dedicated to present the reliability of the code, which includes the simulation of the energy deposition, the shear flow and the Kelvin-Helmholtz instability. Furthermore, a series of material simulations involving X-ray irradiation are conducted in this section to verify the simulation capabilities of the *Xablation2D* code for the BOI. Finally, we arrive at a conclusion in the last section.

II. THEORETICAL BASIS AND MODELING FOR SIMULATION

A. Fluid PIC scheme

We use the Harlow's splitting PIC scheme to solve the hydrodynamic equations. Without loss of generality, the equations can be written as an abstract operator form

$$\frac{\partial \boldsymbol{q}}{\partial t} + \hat{A}\boldsymbol{q} = 0, \tag{1}$$

where $\boldsymbol{q}(\boldsymbol{r}, t)$ is an arbitrary hydrodynamic quantity, and $\hat{A}$ is an abstract operator. According to the rule of operator decomposition, the solution of the equation (1) at the time step Δt is reduced to the sequential solution of two auxiliary problems [28]

$$\begin{cases} \dfrac{\partial \tilde{\boldsymbol{q}}(\boldsymbol{r}, t)}{\partial t} + \hat{E}\tilde{\boldsymbol{q}}(\boldsymbol{r}, t) = 0, \\ \dfrac{\partial \boldsymbol{q}(\boldsymbol{r}, t)}{\partial t} + \hat{L}\boldsymbol{q}(\boldsymbol{r}, t) = 0, \end{cases} \tag{2}$$

where $\hat{A} = \hat{E} + \hat{L}$. The two equations in Eq. 2 correspond to the "Euler step" and "Lagrange step" in the Harlow scheme, respectively. In the "Euler step", the operator $\hat{E}$ does not incorporate the spatial divergence operator, so the equation is easy solved on a fixed spatial grid. In the "Lagrange step", pseudo-particles are introduced to carry mass density, momentum density, and specific internal energy density. In one time step, as the pseudo-particles move to new positions, the new hydrodynamic quantities are obtained on grids by summing up pseudo-particles. The "Lagrange step" can be seen as a computational procedure for modeling particle migration, which compensates for the transport effect that is neglected in the "Euler step".

Without loss of generality, the second equation in Eq. 2 can be written as

$$\frac{\partial \boldsymbol{q}}{\partial t} + \nabla \cdot (\boldsymbol{q}\boldsymbol{U}) = 0, \tag{3}$$

where $\boldsymbol{U}$ is the flow velocity, and $\boldsymbol{q} = (\rho, \rho\boldsymbol{U}, \rho e)$ represents the mass density, momentum density, and internal energy density, respectively. Eq. 3 is the form of the conservation equation, the solution of which can be written as a summation of pseudo-particles

$$\boldsymbol{q}(\boldsymbol{r}, t) = \sum_{j=1}^{N} \boldsymbol{Q}_j R(\boldsymbol{r}, \boldsymbol{r}_j(t)). \tag{4}$$

The total number of pseudo-particles is denoted as N, $\boldsymbol{Q}_j$ represents the carried hydrodynamic quantities of the j-th pseudo-particle. The value of $\boldsymbol{Q}_j$ remains a constant in one "Lagrange step". The kernel function of the pseudo-particle, denoted as $R(\boldsymbol{r}, \boldsymbol{r}_j(t))$, is a function that depends on the current space coordinate $\boldsymbol{r}$ and the radius-vector $\boldsymbol{r}_j$ of the j-th pseudo-particle center. This kernel function satisfies certain universal properties in the usual

$$\begin{cases} R(\boldsymbol{r}_1, \boldsymbol{r}_2) = R(\boldsymbol{r}_2, \boldsymbol{r}_1) \geqslant 0, \\ \dfrac{\partial R}{\partial \boldsymbol{r}_1} = -\dfrac{\partial R}{\partial \boldsymbol{r}_2}, \\ \displaystyle\int_{\Omega} d\boldsymbol{r}_1 R(\boldsymbol{r}_1, \boldsymbol{r}_2) = 1, \end{cases} \tag{5}$$

where Ω denotes the full space. With the aforementioned characteristics and any smooth finite function, the representation $\boldsymbol{q}(\boldsymbol{r}, t)$ in Eq. 4 enables the simplification of Eq. 3 to fulfill the equations of motion for pseudo-particles

$$\frac{d\boldsymbol{r}_j}{dt} = \boldsymbol{U}(\boldsymbol{r}_j(t)), \quad j = 1, 2, \ldots, N. \tag{6}$$

Our code comprises three primary modules: energy deposition module, equation of state (EOS) module and ideal hydrodynamics module, which are complemented by a post-processing script for blow-off impulse calculation to constitute the complete *Xablation2D* code.

B. Energy deposition

The energy deposition module is responsible for estimating the transfer of energy between X-rays and matter. At a microscopic level, X-rays primarily interact with matter through electrons. Initially, the energy of the photons is transferred directly to the electrons, which then interact with atoms in the matter, resulting in energy deposition. Photoelectric effect dominates in the low energy region. With the energy of the photons increases, Compton scattering would contribute [29]. In the case of far-field X-ray irradiation the degree of ionization of the material is so low that effects of plasma could be disregarded. The energy flux for parallel X-rays incident on the target material can be estimated by considering the distance x traveled in the incident direction,

$$\Phi(x) = \Phi_0 \frac{\int_0^\infty f(\lambda, T) \exp[-\mu(\lambda)\rho x] d\lambda}{\int_0^\infty f(\lambda, T) d\lambda}, \tag{7}$$

where Φ_0 and $\Phi(x)$ are energy flux at initial and x position respectively, $f(\lambda, T)$ is the energy spectrum for X-ray, which

depends on the photon wavelength λ and radiation temperature T, ρ is the mass density, $\mu(\lambda)$ is the mass absorption coefficient associated with the photon wavelength. The energy spectrum $f(\lambda, T)$ approximates a black-body spectrum for X-rays produced by a nuclear explosion. In then numerical simulation, it is necessary to truncate and discretize energy spectrum. Hence, the expression of energy flux in computing can be written as,

$$\Phi(x) = \Phi_0 \sum_j w_j \exp[-\mu(\lambda_j)\rho x], \tag{8}$$

where subscript j is the discretized energy group index, w_j represents the proportion of incident energy flux of monochromatic light with a specific wavelength λ_j. The quantity e_R signifies the amount of photon energy deposited through the interaction between X-rays and matter, per unit mass and per unit time, within the region $x \sim x + \Delta x$

$$e_R = \frac{\Phi(x) - \Phi(x + \Delta x)}{\rho \Delta x \tau}, \tag{9}$$

where τ is the time increment. It is postulated that the entirety of the aforementioned deposited energy undergoes conversion into internal energy in the subsequent discuss.

C. Equation of state

X-ray irradiation induces significant changes in the state of matter, including phase transitions, thermal expansion, and shock compression etc, rendering a large range of material parameters. Consequently, it is necessary to employ distinct equations of state to characterize the expansion and compression regions of the material, respectively. For the thermal expansion region, the PUFF EOS [15] is adopted,

$$p = \rho \left[\gamma - 1 + (\Gamma_0 - \gamma + 1)\sqrt{\frac{\rho}{\rho_0}} \right] \left[e - e_s \left\{ 1 - \exp \left[\frac{N\rho_0}{\rho} \left(1 - \frac{\rho_0}{\rho} \right) \right] \right\} \right], \quad \rho < \rho_0, \tag{10}$$

where ρ_0 and ρ are the initial and current density respectively, p is the material pressure, Γ_0 is the Güneisen coefficient, γ is the specific heat ratio of vaporized gas, e_s is the sublimation energy, and $N = C_0^2/\Gamma_0 e_s$. C_0 is a Hugoniot parameter, which determines the shock wave velocity D in solid material with the post-shock velocity u and another Hugoniot parameter λ by

$$D = C_0 + \lambda u. \tag{11}$$

For the compression zone, the Güneisen EOS on the Hugoniot line is used, which is expressed as [30]

$$p = p_H(v) + \rho_0 \Gamma_0 (e - e_H), \quad \rho \geqslant \rho_0, \tag{12}$$

where $p_H(v)$ and e_H are

$$p_H(v) = \frac{\rho_0 C_0^2 (1 - v/v_0)}{[1 - \lambda(1 - v/v_0)^2]} \tag{13}$$

and

$$e_H = \frac{1}{2} p_H(v_0 - v), \tag{14}$$

respectively, which represents the post-shock pressure and specific internal energy when the pre-shock is stationary, respectively, $v = 1/\rho$ is the specific volume, and v_0 is the initial specific volume.

In addition to the analytic expression of EOS, an open-source code, *FEOS*, providing the EOS for a wide range of temperatures and densities in tabular form [31]. FEOS based on the QEOS (quotidian equation of state) model [32], calculates the material specific Helmholtz free energy $F(\rho, T)$ directly, which is widely used in some computational fluid dynamics codes.

D. Ideal hydrodynamics

In this hydrodynamics module, on the one hand we ignore the effects of thermal radiation and heat conduction. The far-field X-ray flux we concerned on the issues is $\mathcal{O}(100 \text{ J/cm}^2)$. In this case the material temperature is $\mathcal{O}(1 \text{ eV})$, and corresponding radiation pressure is only $\mathcal{O}(1 \text{ Pa})$, which is far lower than the material pressure. The velocity of the thermal shock wave in solid materials is about $\mathcal{O}(1 \text{ km/s})$, which is much faster than heat conduction. Therefore, it is reasonable to ignore these effects. In the other hand, our code aims at calculating the blow-off impulse occurring in the thermal expansion vaporized region. This region is characterized by significantly lower material stress compared to the material pressure, thus we can also ignore the stress for impulse calculation in the following.

The 2D governing equations of ideal hydrodynamics are written in the following,

$$\begin{cases} \dfrac{\partial \rho}{\partial t} + \dfrac{\partial}{\partial x}(\rho u_x) + \dfrac{\partial}{\partial y}(\rho u_y) = 0, \\[6pt] \dfrac{\partial}{\partial t}(\rho u_x) + \dfrac{\partial}{\partial x}(\rho u_x^2) + \dfrac{\partial}{\partial y}(\rho u_x u_y) = -\dfrac{\partial p}{\partial x}, \\[6pt] \dfrac{\partial}{\partial t}(\rho u_y) + \dfrac{\partial}{\partial y}(\rho u_y^2) + \dfrac{\partial}{\partial x}(\rho u_x u_y) = -\dfrac{\partial p}{\partial y}, \\[6pt] \dfrac{\partial w}{\partial t} + \dfrac{\partial}{\partial x}(w u_x) + \dfrac{\partial}{\partial y}(w u_y) = e_R, \end{cases} \tag{15}$$

where ρ is the mass density, $\boldsymbol{u} = (u_x, u_y)$ is the fluid velocity, p is the pressure, e is the specific internal energy, $w = \rho(e + \boldsymbol{u}^2/2)$ is the total energy, and e_R is the deposited energy from X-ray irradiation per unit mass per unit time. Account to the

Harlow's splitting scheme, the 2D governing equations can be divided into distinct groups,

$$
\begin{cases}
\dfrac{\partial \rho_1}{\partial t} = 0, \\[2mm]
\dfrac{\partial}{\partial t}(\rho_1 u_{x,1}) = -\dfrac{\partial p}{\partial x}, \\[2mm]
\dfrac{\partial}{\partial t}(\rho_1 u_{y,1}) = -\dfrac{\partial p}{\partial y}, \\[2mm]
\dfrac{\partial w}{\partial t} = -\dfrac{\partial}{\partial x}(p u_{x,1}) - \dfrac{\partial}{\partial y}(p u_{y,1}) + e_R,
\end{cases}
\tag{16}
$$

and

$$
\begin{cases}
\dfrac{\partial \rho_2}{\partial t} + \dfrac{\partial}{\partial x}(\rho_2 u_{x,2}) + \dfrac{\partial}{\partial y}(\rho_2 u_{y,2}) = 0, \\[2mm]
\dfrac{\partial}{\partial t}(\rho_2 u_{x,2}) + \dfrac{\partial}{\partial x}(\rho_2 u_{x,2}^2) + \dfrac{\partial}{\partial y}(\rho_2 u_{x,2} u_{y,2}) = 0, \\[2mm]
\dfrac{\partial}{\partial t}(\rho_2 u_{y,2}) + \dfrac{\partial}{\partial x}(\rho_2 u_{x,2} u_{y,2}) + \dfrac{\partial}{\partial y}(\rho_2 u_{y,2}^2) = 0, \\[2mm]
\dfrac{\partial w_2}{\partial t} + \dfrac{\partial}{\partial x}(u_{x,2} w_2) + \dfrac{\partial}{\partial y}(u_{y,2} w_2) = 0.
\end{cases}
\tag{17}
$$

where subscript 1 and 2 denote "Euler step" and "Lagrange step", respectively.

E. Blow-off impulse calculation

When X-ray irradiates on the material surface, the material undergoes sublimation, forming an evaporation layer. The vaporized material violently ejects outward to the surrounding and generates a blow-off impulse. According to the impulse theorem, the specific impulse in a given direction equals to the change in momentum

$$
I = \int_{P_0}^{P} dP = P - P_0 = m(u - u_0),
\tag{18}
$$

where P, u, P_0 and u_0 represent the final momentum, final flow velocity, initial momentum and initial flow velocity in a certain direction respectively, m is the material mass. Typically, the initial velocity of the vaporized material is zero, that is $u_0 = 0$. For numerical calculations, Eq. 18 can be written as a summation form [33]

$$
I = \sum_{u_j < 0, e_j > e_s} m_j |u_j|,
\tag{19}
$$

where m_j and u_j are the material mass and velocity in the j-th grid respectively, that accounts for the sum of the momentum in all grids in which vaporized material ejects outward. On the other hand, the BOI can also be computed by its definition

$$
I = \int_{t_0}^{t} p_g dt,
\tag{20}
$$

where p_g represents the pressure exerted by the ejected gas on the surface of the solid material at rest, t and t_0 are the final and initial time, respectively. For numerical calculations, the discrete form of Eq. 20 is

$$
I = \sum_{n} p_g \Delta t,
\tag{21}
$$

where n represents the n-th vaporized grid.

III. ALGORITHM IMPLEMENTATION

According to the theoretical framework outlined in Section II, we develop a two-dimensional code, named as *Xablation2D*, to calculate the blow-off impulse of material under far-field X-ray radiation. This section provides a detailed description of the algorithm implemented in *Xablation2D*. In the following discussion, we will omit the subscript 1,2 that distinguishes "Euler step" and "Lagrange step", for convenience.

A. Initialization

We discrete the simulation domain into rectangular grids on the Cartesian coordinate. The physical quantities of the fluid, exception of mass density, are initialized by manually assigned to the grid points. The mass density is initialized by summing up the weight of the pseudo-particles shown as follows,

$$
\begin{aligned}
\rho_{i,j} &= \rho_{i,j} + \rho_p \cdot \omega_{i,j}, \\
\rho_{i+1,j} &= \rho_{i+1,j} + \rho_p \cdot \omega_{i,j}, \\
\rho_{i,j+1} &= \rho_{i,j+1} + \rho_p \cdot \omega_{i,j}, \\
\rho_{i+1,j+1} &= \rho_{i+1,j+1} + \rho_p \cdot \omega_{i,j},
\end{aligned}
\tag{22}
$$

where $\rho_{i,j}$ is the mass density on the grid, ρ_p denotes the mass density carried by the pseudo-particle, and $\omega_{i,j}$ is the weight factor. It is important to note that in our code, the value of ρ_p remains constant throughout the entire simulation. The area-weighting method shown in Fig. 1 is employed to distribute the mass density in the 2D simulation, and weight factors are expressed as

$$
\begin{aligned}
\omega_{i,j} &= \frac{A_1}{A_1 + A_2 + A_3 + A_4}, \\
\omega_{i+1,j} &= \frac{A_2}{A_1 + A_2 + A_3 + A_4}, \\
\omega_{i,j+1} &= \frac{A_3}{A_1 + A_2 + A_3 + A_4}, \\
\omega_{i+1,j+1} &= \frac{A_4}{A_1 + A_2 + A_3 + A_4},
\end{aligned}
\tag{23}
$$

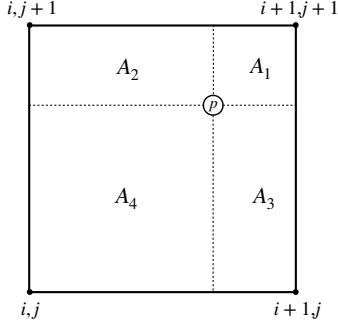where A_i ($i = 1, 2, 3, 4$) represents the area of overlap between the pseudo-particle and the grid.

Fig. 1. Area-weighting method for the pseudo-particle in 2D simulation. The circle p represents the pseudo-particle center, and the black dot (i,j) is the grid point.

B. Euler step

The radiative deposition energy and equation of state are discretized on the grid in the following,

$$e_{R,i,j}^n = \frac{\Phi_{i-1,j-1}^n - \Phi_{i,j}^n}{\rho_{i,j}^n h_1 \tau}, \qquad (24)$$

and

$$\begin{cases} p_{i,j}^n = p_{H,i,j}^n \\ \qquad + \Gamma_0 \rho_0 \left[e_{i,j}^n - \frac{1}{2} p_{H,i,j}^n (v_0 - v_{i,j}^n) \right], \quad \rho_{i,j} \geqslant \rho_0, \\ p_{i,j}^n = \rho_{i,j}^n \\ \qquad \times \left[\gamma - 1(\Gamma_0 - \gamma + 1)\sqrt{\frac{\rho_{i,j}^n}{\rho_0}} \right] e_{A,i,j}^n, \quad \rho_{i,j} < \rho_0, \end{cases} \qquad (25)$$

where $p_{H,i,j}^n$ and $e_{A,i,j}^n$ are

$$p_{H,i,j}^n = \frac{\rho_0 C_0^2 (1 - v_{i,j}^n/v_0)}{[1 - \lambda(1 - v_{i,j}^n/v_0)^2]}, \qquad (26)$$

and

$$e_{A,i,j}^n = e_{i,j}^n - e_s \left\{ 1 - \exp\left[\frac{N\rho_0}{\rho_{i,j}^n}(1 - \frac{\rho_0}{\rho_{i,j}^n}) \right] \right\}, \qquad (27)$$

respectively. Then hydrodynamic equations (Eq. 16) in the "Euler step" can be discretized as

$$\begin{cases} u_{x,i,j}^{n+1} = u_{x,i,j}^n - \frac{\tau}{h_1 \rho_{i,j}^n}(p_{i+1/2,j}^n - p_{i-1/2,j}^n), \\ u_{y,i,j}^{n+1} = u_{y,i,j}^n - \frac{\tau}{h_2 \rho_{i,j}^n}(p_{i,j+1/2}^n - p_{i,j-1/2,j}^n), \\ e_{i,j}^{n+1} = e_{i,j}^n - \frac{\tau p_{i,j}^n}{\rho_{i,j}^n}\left(\frac{u_{x,i+1/2,j}^n - u_{x,i-1/2,j}^n}{h_1} \right. \\ \qquad \left. + \frac{u_{y,i,j+1/2}^n - u_{y,i,j-1/2}^n}{h_2} \right) + e_{R,i,j}^n, \end{cases} \qquad (28)$$

where subscript (i,j) denotes the grid index in the spatial coordinate system, the superscript n represents the n-th time step, τ is the time increment, h_1 and h_2 are the grid sizes in the x and y direction, respectively. Note that the mass density remains constant as shown in Eq. 16, that is $\rho_{i,j}^{n+1} = \rho_{i,j}^n$.

C. Lagrange step

In the "Lagrange step", the fluid is divided into many pseudo-particles with finite sizes. We assume an internal distribution function of fluid quantities within a pseudo-particle [34]

$$q(\xi, \eta) = \{(q_{i+1,j+1} - q_{i+1,j})(2\eta - \delta\eta) + q_{i+1,j}\}(2\xi - \delta\xi) - \{(q_{i,j+1} - q_{i,j})(2\eta - \delta\eta) + q_{i,j}\}(2\xi - \delta\xi - 1), \qquad (29)$$

where the pseudo-particle size is normalized, $q(\xi, \eta)$ is the physical quantity carried by the pseudo-particles[5], the coordinates (ξ, η) represent the internal position within the pseudo-particle, with the origin located at the bottom left-hand corner, and $(\delta\xi, \delta\eta)$ are intervals from the origin of the internal coordinate system to the boundaries of the grid in the x and y directions, respectively. These are illustrated in Fig. 2, where the red lines represent the grids, the red dot represents the pseudo-particle center, and the blue square represents the pseudo-particle size. q_p represents the physical quantity carried by the pseudo-particle located at the internal coordinate center, which can be obtained by integrating $q(\xi, \eta)$ from 0 to 1

---

[5] q only represents the velocity $\boldsymbol{u} = (u_x, u_y)$ and specific internal energy e of the pseudo-particle, not mass density ρ, which has been set to constant ρ_p in the initialization.
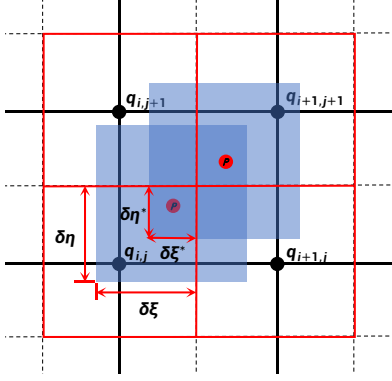
Fig. 2. A distribution of quantities within a pseudo-particle. The red dot p represents the pseudo-particle center, the blue square represents the pseudo-particle size, and the black dot is the grid point. The label * represents the interval when the pseudo-particle reaches a new position.

$$
\begin{aligned}
q_p &= \int_0^1 \int_0^1 q(\xi, \eta) d\xi d\eta \\
&= q_{i+1,j+1}(1 - \delta\xi)(1 - \delta\eta) \qquad (30) \\
&\quad + q_{i+1,j}(1 - \delta\xi)\delta\eta + q_{i,j+1}\delta\xi(1 - \delta\eta) + q_{i,j}\delta\xi\delta\eta \\
&= q(\frac{1}{2}, \frac{1}{2}).
\end{aligned}
$$

The equations of pseudo-particle motion are

$$
\begin{cases}
x_p^{n+1} = x_p^n + \tau u_{p,x}, \\
y_p^{n+1} = y_p^n + \tau u_{p,y},
\end{cases} \qquad (31)
$$

where (x_p, y_p) denote the position of the pseudo-particle center, and $(u_{p,x}, u_{p,y})$ represent the velocity of the pseudo-particle center, as determined by Eq. 30. When the pseudo-particle has been advanced and reaches a new position as shown in Fig. 2, we recompute the new intervals from the origin of the internal coordinate, denoted as $(\delta\xi^*, \delta\eta^*)$. By summing pseudo-particles at new positions, new fluid quantities on the grid can be derived. In this paper, we present three algorithms, Area-weighting method (AWM), Integration-weighting method (IWM) and Interpolation-Integration-weighting method (IIWM), for the summation process, each of which exhibits different types of numerical diffusion [34]. The details of summation algorithms are shown in Appendix A. The three algorithms have different numerical diffusion and noise, and can be selected according to the requirements of actual problems.

D. Parallelization

The Massage Passing Interface (MPI) is employed in the construction of parallelization [35]. The details of parallel communication are shown in Appendix B.

IV. SIMULATION RESULTS

A. Far-field X-ray energy deposition

The module of X-ray energy deposition is crucial for the calculation accuracy of the blow-off impulse in *Xablation2D* code. To validate this module, we compared the energy deposition rate from *Xablation2D* code with those obtained from Monte Carlo code, *Geant4* [36–39]. In the *Xablation2D* simulation, the parallel soft X-rays, with an initial energy flux $\phi_0 = 418$ J/cm^2, are incident perpendicularly into a 2D planar aluminum (Al) target, with a density $\rho = 2.738$ g/cm^3, and the pulse duration is 50 ns. The energy spectrum of the X-rays approximates a black-body spectrum with the radiation temperature $T = 1$ keV. The range of wavelength in energy spectrum is $\lambda = 0.1$ Å to 10 Å, discretized into 23 energy groups for numerical simulation. The mass absorption coefficient μ in the Al material for X-rays in each energy group is shown in the Tab. 1.

In the *Geant4* code, a parallel black body spectrum photon beam with the radiation temperature 1 keV is configured to simulate soft X-rays. The interaction between photons and materials is simulated by the Livermore low-energy electromagnetic physics model, which is effective within the energy range of the photon from 250 eV to 1 GeV. By tracking the trajectory of photons within the Al target, it is possible to quantify the amount of the deposition energy in the material. The energy deposition rates calculated by the two code are shown in Fig. 3, where the vertical axis corresponds to the energy deposition rate, which signifies the lost ratio of the incident energy flux after traversing corresponding distance in the material, and the horizontal axis represents the depth within the aluminum target, along with the direction of the incident X-rays. Fig. 3 also shows the relative error of the two results by orange dashed line. It is observed that there is the largest deviation near the material surface, and then rapidly decreases to $\mathcal{O}(5\%)$ along the incident depth. The reason is that the value of the energy deposition rate is small at the material surface, where even a minor deviation on parameters, such as the mass absorption coefficients in the database, can result in a noticeable relative error. In addition, the depth required for 50% X-ray energy to be deposited in the material is 4.17 μm for *Xablation2D* and 3.5 μm for *Geant4*, respectively, which is consistent with $\mathcal{O}(5 \ \mu$m) estimated in [19].

B. Shear flow simulation

We use the plane shear flow simulations to verify the numerical diffusion from the algorithms of AWM, IWM and IIWM. In the *Xablation2D* code, the size of the simulation domain is $L_x \times L_y = 0.4 \times 0.4$ cm^2, and the domain is discretized into 400×400 grids. 10×10 pseudo-particles are allocated for each grid. The whole flow field is divided into two layers. The upper fluid is denoted as A and the lower fluid as B. The interface between the two fluids is located at $y = 0.2$ cm. The mass density, velocity in the x

λ (Å)	0.1	0.15	0.2	0.25	0.3	0.4	0.5	0.6	0.7	0.8	0.9	1.0
μ (cm^2/g)	0.155	0.205	0.277	0.38	0.525	0.97	1.82	3.7	5.75	8.8	11.8	15.2

λ (Å)	1.5	2.0	2.5	3	4	5	6	7	8	9	10	
μ (cm^2/g)	41.5	87	235	360	780	1400	2250	3300	280	390	520	

TABLE 1. Discretized black-body spectrum from wavelength $\lambda = 0.1$ Å to 10 Å and corresponding mass absorption coefficient μ in the Al material [19].
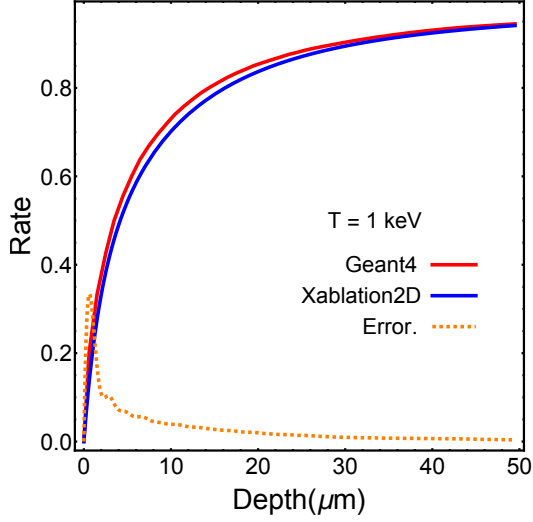
Fig. 3. The energy deposition rate varying with the material depth along the X-rays incident direction.

direction and velocity in the y direction of the upper fluid are $\rho_A = 2.738$ g/cm^3, $u_{Ax} = 3 \times 10^5$ cm/s and $u_{Ay} = 0$ cm/s, respectively. The lower fluid has the same mass density as the upper $\rho_B = \rho_A$, a velocity is equal in magnitude but opposite in the x direction $u_{Bx} = -u_{Ax}$, and the same velocity in the y direction $u_{By} = u_{Ay}$. The simulation employs the periodic boundary condition in the x direction, and the open boundary condition in the y direction. In addition, the ideal gas EOS is adopted,

$$p = (\gamma - 1)\rho e, \qquad (32)$$

where $\gamma = 1.667$ is the ratio of specific heat, the initial pressure p is set to 1 GPa. The fluid velocity distribution in the x direction (u_x) of shear flow is shown in Fig. 4.

In Fig. 4, it can be observed that the IIWM (or IWM) has a better suppression for numerical diffusion than that of the AWM. For the AWM in Fig.4 (a), the jumped shear flow velocity becomes smooth, and this smoothness gradually saturates into the upper and lower layers due to numerical diffusion, but for the IIWM (or IWM) in Fig.4 (b), the jumped velocity can be maintained throughout the entire simulation time due to using the integration of the internal distribution function in the shear velocity direction.

C. Kelvin-Helmholtz instability simulation

When two contiguous fluids flow with shear velocities, an instability can arise at the interface between the fluids as long as there is a small fluctuation. This phenomenon is known as the Kelvin-Helmholtz instability (KHI) [40, 41]. KHI is widely observed in natural, including the turbulent mixing of fluids in jet streams, the formation of undulates clouds and supernova explosions [42–44]. Here, we performed the KHI simulations by the *Xablation2D* code and the open radiation magnetohydrodynamics simulation code *FLASH4* [45] respectively, and compared the two simulation results. The initial parameters, including the size of the simulation domain, the number of grids, and the number of pseudo-particles for each grid, are the same as the Section IV B, except for temperature. The initial material temperature is set to $T = 21.6$ eV, corresponding to the specific internal energy $e = 1 \times 10^5$ J/g. The initial pressure determined by EOS is 182.24 GPa. Initially, a velocity perturbation in the y direction is introduced at the interface of the two fluids as a seed for KHI in the following form [46]

$$u_y^1 = u_0 \sin(kx - \frac{\pi}{2})e^{(k|y - \frac{L_y}{2}|)}, \qquad (33)$$

where $u_0 = 1 \times 10^6$ cm/s is the initial amplitude, $k = 4\pi/L_x$ cm^{-1} is the initial wave number. In order to observe secondary unstable structures of KHI, it is necessary to reduce numerical diffusion, so we adopt the IWM in the *Xablation2D* simulation. In the *FLASH4* simulation, we maintain consistency in the initialization parameters and perturbation, but use the adaptive mesh refinement (AMR).

Fig. 5 illustrates the mass density the evolution of the lower half fluid. The six subfigures in the first row are the results obtained from *Xablation2D* code, and the second row from *FLASH4* code. The simulation results of the two codes are consistent. It can be observed that the disturbance at the fluid interface gradually increases, and eventually, the two fluids mix and show vortex structures. The IIWM is also employed to simulate KHI process with the same parameter in the *Xablation2D*. The simulation results are basically consistent with *FLASH4*, except for some secondary structures, as shown in Fig. 6. This deviation can be attributed to the relatively higher numerical diffusion in the direction of convective velocity in the IIWM.

The mixing width η is defined as the difference between the maximum position and the initial position of the lower half fluid, as shown in Fig. 7 (a). The evolution of the mixing width is shown in Fig. 7 (b), where the blue and
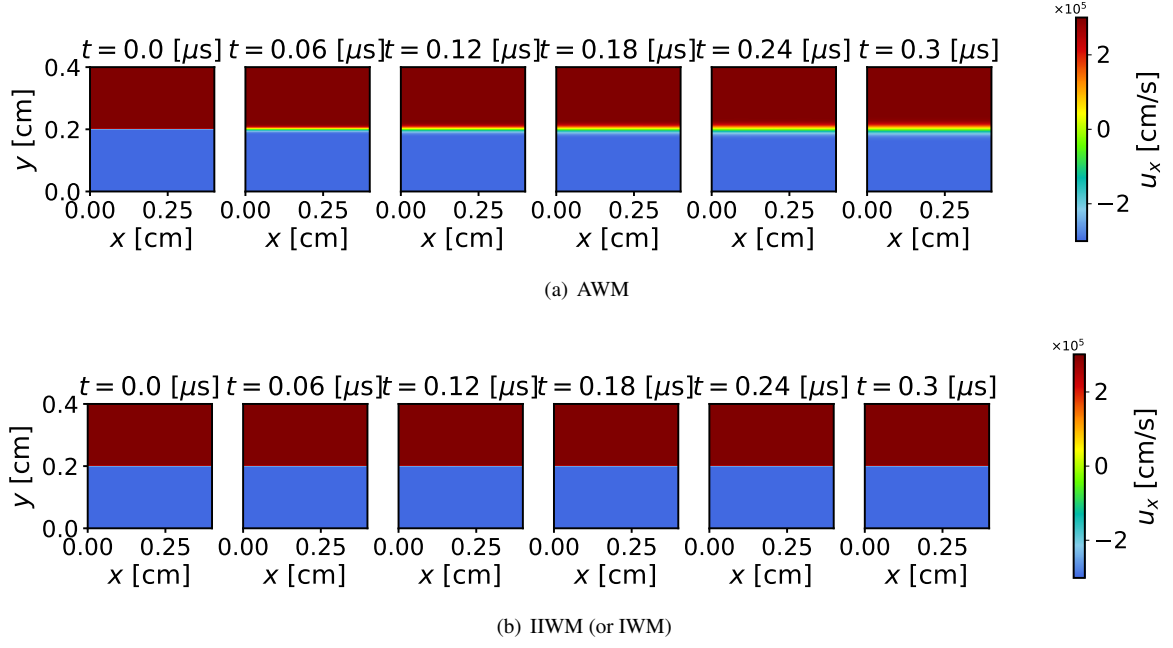
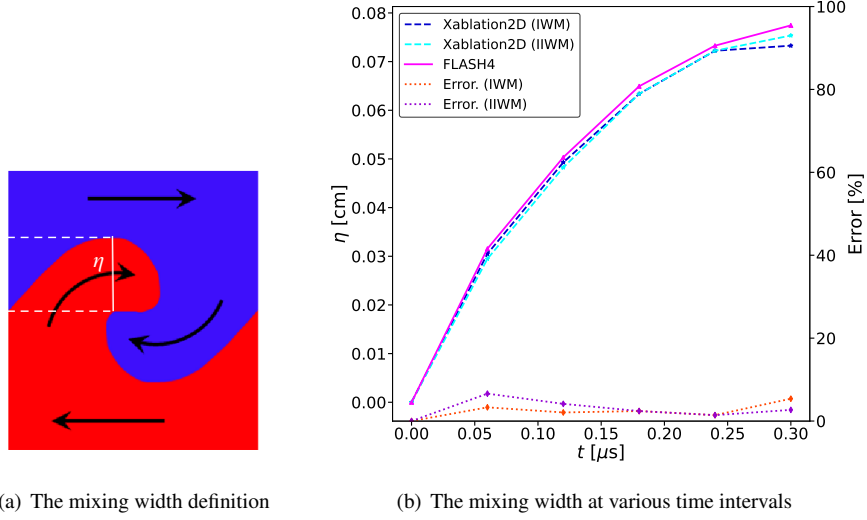(a) The mixing width definition   (b) The mixing width at various time intervals
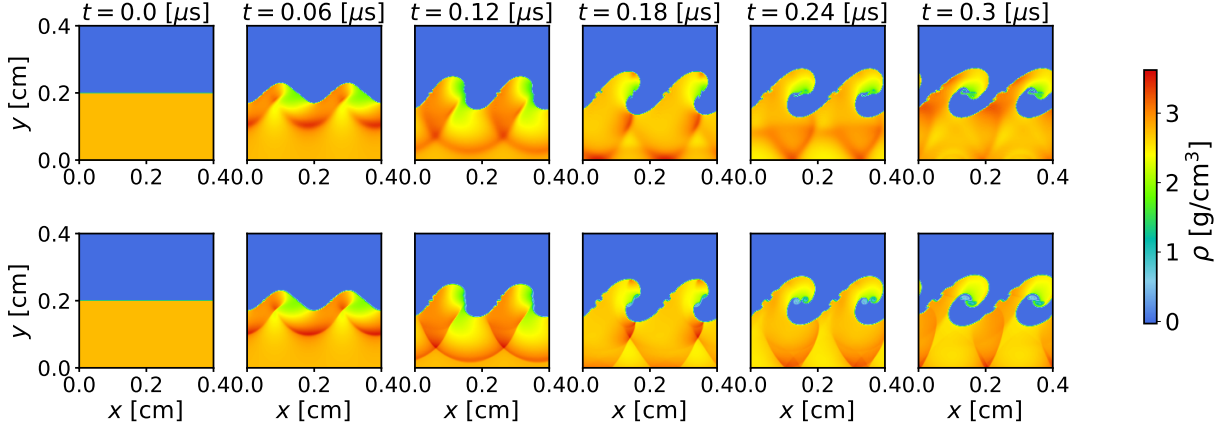
Fig. 7. The evolution of the mixing width and relative error in the *Xablation2D* and *FLASH4* simulations, respectively.

FLASH4. The orange dotted lines indicate relative errors between two codes, which remain $\mathcal{O}(5\%)$, indicating a certain level of consistency between the two codes. This minor deviation validates the reliability of the *Xablation2D* code. It is observed that the growth of the mixing width is significantly smaller than what is predicted by classical linear theory of the KHI. The reason is that the compressibility of the simulation and the evolution of the fluid is non-linear due to the strong initial perturbation.

D. Vaporization blow-off impulse

When X-rays irradiate the solid material, a blow-off impulse will load on the material surface, as illustrated in Fig. 8. The energy of the photons in X-rays is primarily absorbed by the material through the photoelectric effect and Compton scattering. The X-ray energy flux decreases exponentially as it penetrates from the surface into the interior of the material. As a result, the specific internal energy of the material at the surface is increasing rapidly, which leads to phase transition and adiabatic expansion, and finally generates an ablation layer. If the deposited energy exceeds the sublimation energy of the material, the solid material at the surface changes into gas, and forms vaporization zone on the front. The vaporized material is sprayed into vacuum violently, and generates a recoil impulse loading on the remaining material, where the recoil impulse is known as the blow-off impulse (BOI).

In the BOI simulation case, the aluminium (Al) material is selected as the target material, the IIWM algorithm is employed in the *Xablation2D* code. The expansion and compression of material are described by PUFF EOS (Eq. 10) and Güneisen EOS (Eq. 12), as discussed in Section II C. The physical property parameters of the Al material in the simulation are shown in the Tab. 2. The simulation domain has a
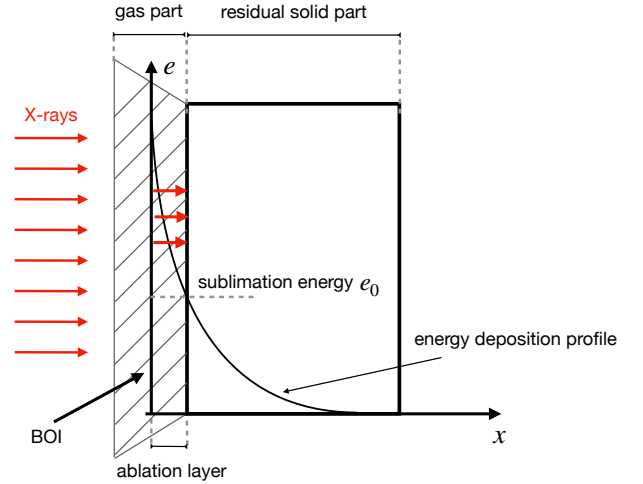

Fig. 8. A simple illustration of the far-field X-ray ablation. The shaded area represents the blow-off impulse, and the black solid curve is the energy deposition curve.

size of $L_x \times L_y = 0.8 \times 0.8\,\mathrm{cm}^2$, and is divided into 400×400 grids. We allocate 100×100 pseudo-particles for each grid near the surface of the target material, while 5×5 pseudo-particles in other region. Two different geometric configurations of the target are simulated, one is a semi-infinite slab and the other is a cylinder.

ρ_0 (g/cm^3)	2.738	Y_0 (GPa)	0.7	e_s (kJ/g)	10.89
C_0 (mm/μs)	5.328	G (GPa)	27	γ	1.667
λ	1.338	Γ_0	2.18	N	1.265

TABLE 2. The physical property parameters of the Al material in the simulation. ρ_0 is the mass density at at room temperature and atmospheric pressure, G is the shear modulus, Y_0 is the yield strength, e_s is the sublimation energy, γ is the specific heat ratio, Γ_0 is the Grüneisen coefficient, λ and C_0 are Hugoniot parameters, and $N = C_0^2/\Gamma_0 e_s$.

1. *Semi-Infinite Slab*

The semi-Infinite slab is located in the region where $x > 0.4$ cm, while the region where $x \leqslant 0.4$ cm is filled with low-density gas to maintain the numerical stability of the code. The periodic boundary condition is applied in the y direction, and the open boundary condition is applied in the x direction. The parallel X-rays have a radiation temperature $T = 1$ keV, and incident on the slab along the normal direction. The energy spectrum is discretized into 23 energy groups as in Tab. 1. The pulse duration and initial energy flux are 50 ns and 418 J/cm^2, respectively. Fig. 9 illustrates the evolution of the mass density and pressure. It is observed that the material surface is vaporized by the X-rays irradiation, and then expand outward into surroundings. The material expanding generates a blow-off impulse (BOI), and gives rise to a thermal shock wave propagating inward. The accumulation of density in the left region is a consequence of the presence of low-density gas in the initialization.

For the semi-infinite slab configuration, the impulse distribution is uniform in the y direction, it is possible to obtain the evolution of one-dimensional average BOI by integrating it along the y direction, and dividing it by the length L_y. This result shown as the blue dashed line in Fig. 10. To verify its correctness, we develop a one-dimensional Lagrangian code referred to Ref. [47] to calculate the BOI under the same parameters. The result is shown as the magenta solid line, which is consistent with the *Xablation2D* code. In addition, we also compare the simulation results with three BOI models shown as the dotted lines in Fig. 10. Their analytical formulas are written as follows [9],

$$
\begin{aligned}
\text{BBAY}: \quad & \mathrm{I} = \alpha\sqrt{2}\left\{\int_0^{x_0}[e(x)-e_s]\,\rho_0 x\,\mathrm{d}x\right\}^{1/2}, \\
\text{Whitener}: \quad & \mathrm{I} = \sqrt{2}\int_0^{x_0}[e(x)-e_s]^{1/2}\,\rho_0\,\mathrm{d}x, \\
\text{MBBAY}: \quad & \mathrm{I} = \alpha\sqrt{2}\left\{\int_0^{x_0}e(x)-e_m\left[1+\ln\frac{e(x)}{e_m}\right]\rho_0^2 x\,\mathrm{d}x\right\}^{1/2},
\end{aligned}
\tag{34}
$$

where $e(x)$ is energy deposition profile, e_m represents the melting energy, α is a correction parameter ranging from 1 to $\sqrt{2}$, and x_0 is the thickness of the sublimation layer determined by setting $e(x) = e_s$. In the simulation, we set $e_m = 3.975$ kJ/g and $\alpha = 1.1$, respectively. It should be noted that the BOI models only estimate the instantaneous deposition energy for irradiation, resulting in horizontal dotted lines in Fig. 10. While the BOIs calculated by the *Xablation2D* and 1D Lagrangian codes, shown as the blue dashed and magenta solid lines in Fig. 10, has a growth time of $\mathcal{O}(0.1\,\mu\mathrm{s})$, it demonstrates a tendency to stabilize, which corresponds to the characteristic time in which the material completely sublimates at the surface. It is also observed that the results obtained from the BBAY model and MBBAY model align well with the stable values of the numerical simulations.

Furthermore, we compared the simulation results of the *Xablation2D* code with the published experimental results to verify the reliability of the code. The Ref. [48] provides three measurements of the BOI produced by X-rays irradiating a flat Al material.The X-ray parameters and measured impulse values in experiments are presented in the Tab. 3. We simulate these three experiments by *Xablation2D* with the experimental parameters. The BOIs of the simulations are shown in Fig. 11 (a). The stable values of these BOIs are 97.84, 121.82, 125.36 Pa·s, respectively. Fig. 11 (b) shows the comparison between the simulation results and the measured BOIs. It is observed that there are two consistent BOIs, and the relative error between the simulation and the experimental results are negligible in case of No.01154 and No.01170. Although the relative error in case of No.01171 is larger, it is still within $\mathcal{O}(20\%)$.

Number	01154	01170	01171
Radiation temperature T (keV)	0.21	0.227	0.211
Pulse duration τ_0 (ns)	53	36	44
Initial flux Φ_0 (J/cm^2)	163	181	192
Measuring impulse I (Pa $\cdot$ s)	99.1	118.5	162.2

TABLE 3. The X-ray parameters and measuring impulse in experiments.

(a) The mass density varying with the simulation time

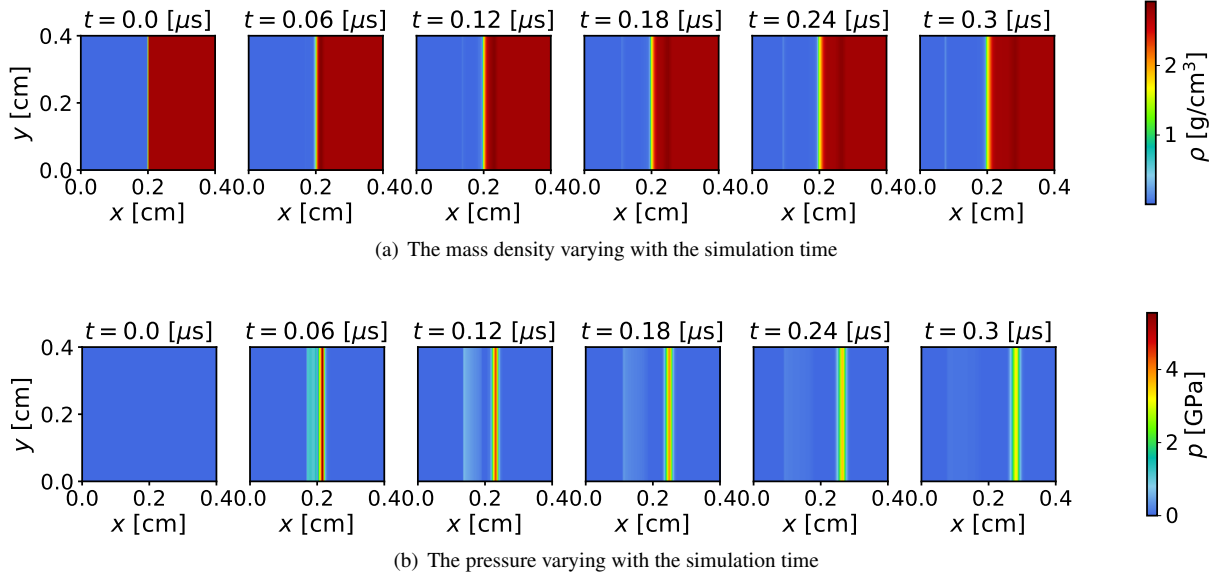(b) The pressure varying with the simulation time

Fig. 9. The mass density and pressure distribution in the semi-inifnite slab at various time intervals.
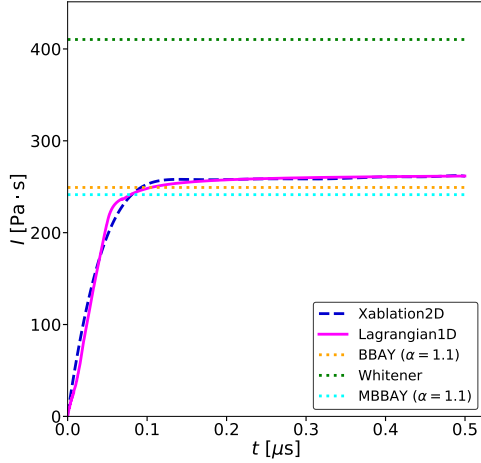

Fig. 10. The blow-off impulse varying with the simulation time.

2. *Cylinder*

In the cylinder configuration, the target is positioned in the center of the simulation domain. The central coordinates of the cylinder is at $x = y = 0.4\,\mathrm{cm}$, and the radius of the target is 0.2 cm. The remaining areas of the simulation domain are filled with a low-density gas. The physical property parameters and X-ray parameters used in this configuration are identical to those employed in the semi-infinite slab configuration. The mass density and pressure distribution in the simulation are shown in Fig. 12. The X-ray irradiates the left side of the cylinder. The vaporized material is produced on the left surface, ejects violently, and generates the BOI, which drives a

thermal shock wave moving toward the center of the cylinder. When the parallel X-ray irradiates on a curved surface, the density of the deposited energy at the material surface is non-uniform. The BOI should be a function of the radial direction of the cylinder. Refs. [10, 11, 21, 49] propose that if the energy deposition density has a cosine profile on the cylinder surface, the variation of the BOI is proportional to the cosine of the polar angle

$$I = I_0 \cdot \cos\theta, \qquad (35)$$

where θ is the polar angle defined in Fig. 13 (a), I_0 represents the BOI at the $\theta = 0°$.

Fig. 13 (b), (c), and (d) show the distribution of the BOI via the polar angle at different time intervals. The BOI profiles basically satisfies the cosine law, but small deviations are also exist. The main reason is that the thickness of X-ray energy deposition cannot be completely ignored. The deviation between the BOI curve and the cosine function increases as the polar angle increases from $0°$ to $90°$, especially at $\theta = 90°$, where specific internal energy of the material is not zero due to the penetration of X-rays into the material, so the BOI is also not zero. The simulation results confirm this phenomenon.

V. CONCLUSION

We develop a novel parallel two-dimensional PIC code, *Xablation2D*, for calculating the BOI of far-field X-ray irradiating materials. The code is mainly composed of three modules: energy deposition module, EOS module and ideal hydrodynamics module. In ideal hydrodynamics module, the solution of hydrodynamics equations is divided into two steps: "Euler step" and "Lagrange step" according to the
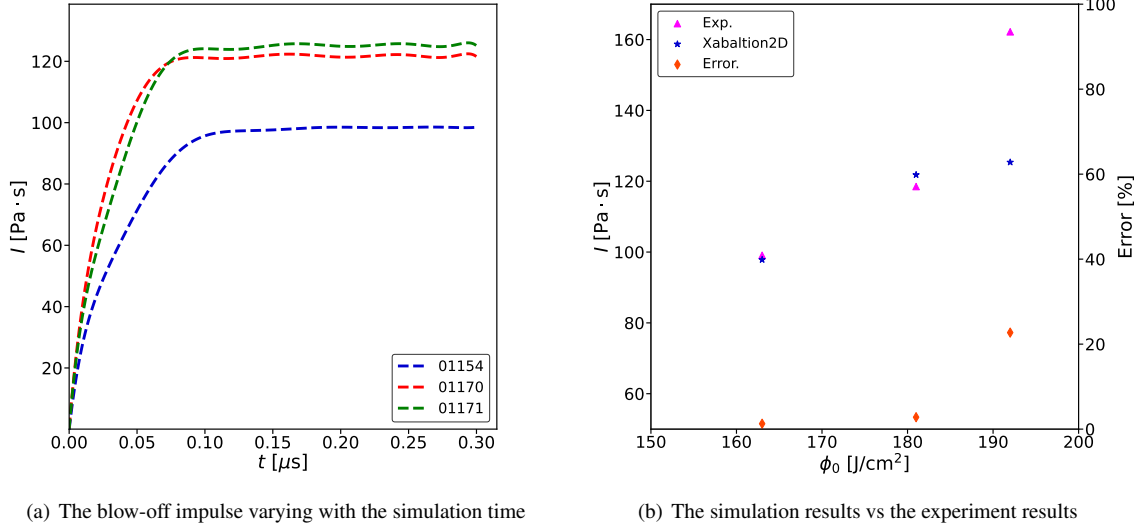
12

(a) The blow-off impulse varying with the simulation time

(b) The simulation results vs the experiment results

Fig. 11. Comparison between the *Xablation2D* simulations and experiments.

(a) The mass density varying with the simulation time
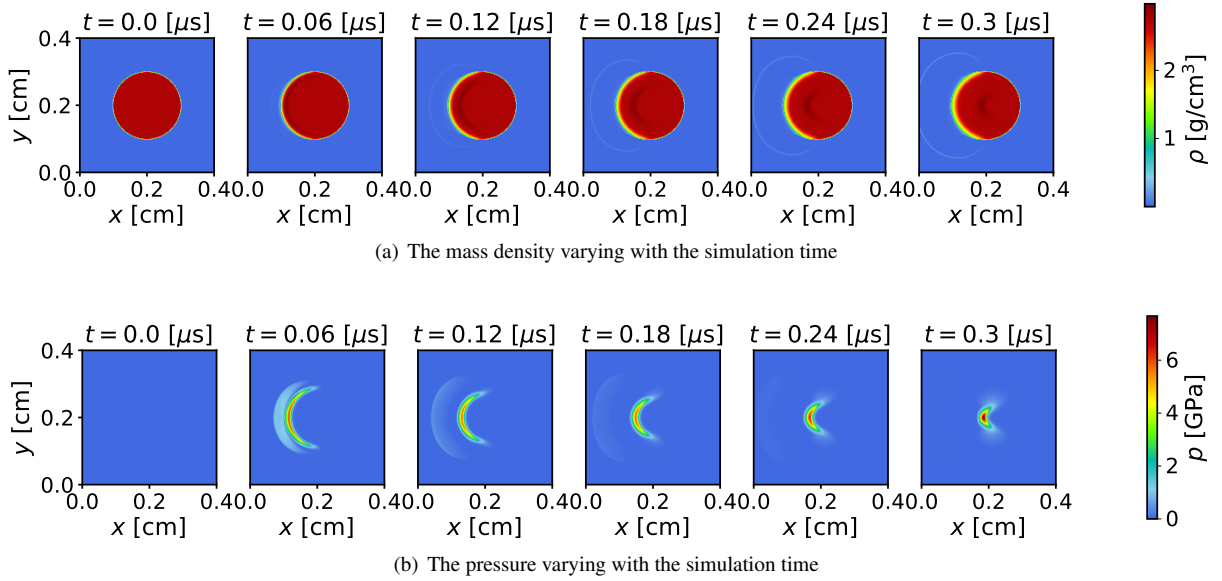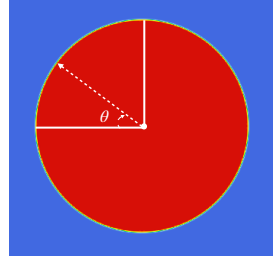

(b) The pressure varying with the simulation time

Fig. 12. The mass density and pressure distribution in the cylinder at various time intervals.

Harlow's splitting scheme. The introduced pseudo-particle is responsible for compensating for the transport effect. We present three new summation algorithms, AWM, IWM and IIWM, to map the physical quantity carried by the pseudo-particle into the grid. In contrast to the conventional finite difference or finite element methods, the new PIC method significantly reduces the dependence on grid shape and is well-suited for the calculation of large deformation problems in materials with complex configurations. In order to verify the reliability of the *Xablation2D* code, we use some open-source codes for comparison. The soft X-ray energy deposition rate is simulated by *Geant4*, and the shear flow and the KHI prob-

lems are simulated by *FLASH4*, respectively. The simulation results exhibit a minor discrepancy compared to our code. Finally, we calculate the BOI in two geometric configurations of the Al materials under far-field X-ray irradiation. The results are well consistent with experimental, analytical, and other simulation results. It is also observed that a thermal shock wave propagates inside the material caused by X-ray irradiation.

For X-rays with increased energy flux, the overall process becomes more intricate. The material will be highly ionized, and the energy deposition process involves the interaction between the radiation field and the plasma. In the future work,
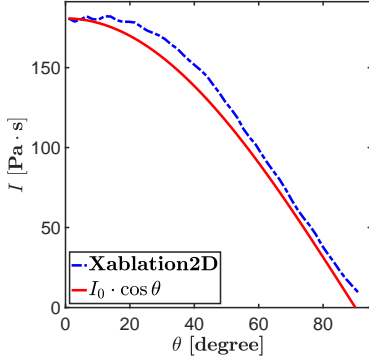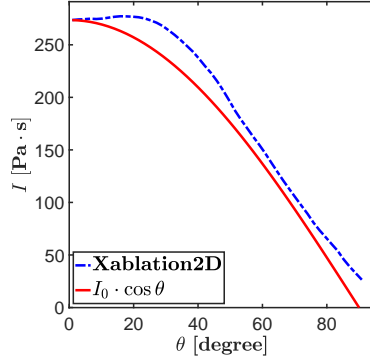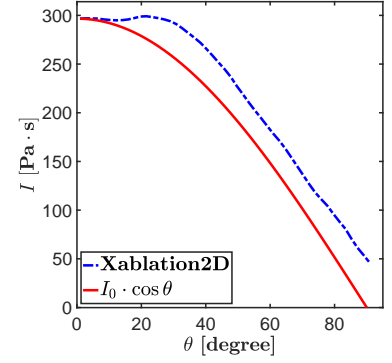
(a) The definition of the polar angle

(b) $t = 0.04\,\mu$s

(c) $t = 0.10\,\mu$s

(d) $t = 0.16\,\mu$s

Fig. 13. The blow-off impulse varying with the polar angle at various time intervals.

we plan to develop a radiation transport module in the *Xablation2D* code for the simulation of ultra-intense X-ray irradiating materials.

Appendix A: Summation algorithms

(1) **Area-weighting method (AWM)**: This approach assumes that the distribution function of the physical quantity $q(\xi, \eta)$ carried by the pseudo-particle collapses into the value located at the internal coordinate center, that is q_p. Therefore, the new fluid physical quantities on the grid can be simply obtained by a summation of the prod- uct of q_p and area as follows,

$$
\begin{aligned}
(\rho q)_{i,j} &= \sum_{p \in (i,j)} \rho_p q_p \delta\xi^* \delta\eta^*, \\
(\rho q)_{i+1,j} &= \sum_{p \in (i+1,j)} \rho_p q_p (1 - \delta\xi^*)\delta\eta^*, \\
(\rho q)_{i,j+1} &= \sum_{p \in (i,j+1)} \rho_p q_p \delta\xi^* (1 - \delta\eta^*), \\
(\rho q)_{i+1,j+1} &= \sum_{p \in (i+1,j+1)} \rho_p q_p (1 - \delta\xi^*)(1 - \delta\eta^*).
\end{aligned}
\tag{A1}
$$

Where $p \in (i,j)$ denotes the pseudo-particle whose center is located in the (i,j) grid. The AWM is a straightforward approach and has high computational efficiency, but introduce zero order numerical diffusion effects.

(2) **Integration-weighting method (IWM)**: The IWM maintains the internal distribution function $q(\xi, \eta)$ during the motion of the pseudo-particle. The new physical quantities on the grid can be obtained by integrating the function $q(\xi, \eta)$ over each new area. This area is defined by the overlap of the pseudo-particle size and the grid. For instance, the area of overlap between the pseudo-particle size and the (i,j) grid can be represented by $\delta\xi^* \times \delta\eta^*$ as shown in Fig. 2. As a result, the new fluid physical

quantities on the grid are written as

$$(\rho q)_{i,j} = \sum_{p\in(i,j)} \rho_p \int_0^{\delta\xi^*} \int_0^{\delta\eta^*} q(\xi,\eta)d\xi d\eta,$$

$$(\rho q)_{i+1,j} = \sum_{p\in(i+1,j)} \rho_p \int_{\delta\xi^*}^1 \int_0^{\delta\eta^*} q(\xi,\eta)d\xi d\eta,$$

$$(\rho q)_{i,j+1} = \sum_{p\in(i,j+1)} \rho_p \int_0^{\delta\xi^*} \int_{\delta\eta^*}^1 q(\xi,\eta)d\xi d\eta,$$ (A2)

$$(\rho q)_{i+1,j+1} = \sum_{p\in(i+1,j+1)} \rho_p \int_{\delta\xi^*}^1 \int_{\delta\eta^*}^1 q(\xi,\eta)d\xi d\eta.$$

The IWM has the second-order numerical diffusion, which is much better than that of the AWM. However, this approach would introduce some non-physical numerical noise, causing the fluid motion become somewhat unstable.

(3) **Interpolation-Integration-weighting method (IIWM)**: The IIWM is a combination of the AWM (used in the convective velocity direction) and IWM (used in the shear velocity direction). For instance, if the $q(\xi,\eta)$ represents the fluid velocity in the x direction (u_x), then an inverse linear interpolation is employed to $q(\xi,\eta)$ in the x direction, and followed by the integration of $q(\xi,\eta)$ in the y direction. The specific procedure are as follows. Initially, we integrates the $q(\xi,\eta)$ over ξ from 0 to 1,

$$\begin{aligned} q(\eta) &= \int_0^1 q(\xi,\eta)d\xi \\ &= \{[q_{i+1,j+1}(1-\delta\xi) + q_{i,j+1}\delta\xi] \\ &\quad - [q_{i+1,j}(1-\delta\xi) + q_{i,j}\delta\xi]\}(2\eta - \delta\eta) \\ &\quad + q_{i+1,j}(1-\delta\xi) + q_{i,j}\delta\xi \\ &= q(\tfrac{1}{2},\eta). \end{aligned}$$ (A3)

Then, we integrate $q(\eta)$ over the length where the overlap of the pseudo-particle size and the grid in the y direction, as shown in Fig. 2, to obtain two new intermediate physical quantities

$$q_1^* = \int_0^{\delta\eta^*} q(\eta)d\eta, \quad q_2^* = \int_{\delta\eta^*}^1 q(\eta)d\eta.$$ (A4)

Finally, new physical quantities are determined by

$$\begin{aligned} (\rho q)_{i,j} &= \sum_{p\in(i,j)} \rho_p q_1^* \delta\xi^*, \\ (\rho q)_{i+1,j} &= \sum_{p\in(i+1,j)} \rho_p q_1^* (1-\delta\xi^*), \\ (\rho q)_{i,j+1} &= \sum_{p\in(i,j+1)} \rho_p q_2^* \delta\xi^*, \\ (\rho q)_{i+1,j+1} &= \sum_{p\in(i+1,j+1)} \rho_p q_2^* (1-\delta\xi^*). \end{aligned}$$ (A5)

Similarly, we can also implement this approach for the fluid velocity in the y direction (u_y).

Appendix B: Parallel communication

MPI adopts an explicit message passing architecture, necessitating the explicit sending and receiving of messages to facilitate data exchange among processors.Each individual parallel process possesses its own memory space. Processors access the memory space of each other through explicit message passing. This design exhibits robust parallelism and is particularly well-suited for the implementation of large-scale parallel algorithms.
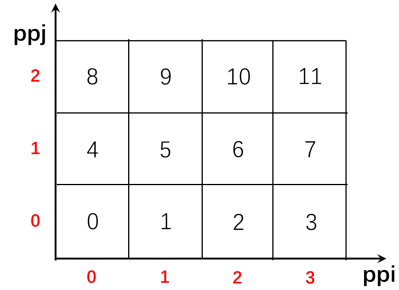

Fig. 14. The parallel division of the simulation region. A total of $N = 12$ processes, numbered from 0 to 11, are assigned to the simulation regions. The number of processes assigned to the grid along the x and y direction are 4 and 3, respectively.

In our code, the simulation region is divided into N parts based on a grid structure, and each part is assigned to a individual process for calculation. The total number of processes $N = ppx \times ppy$, where ppx and ppy are the number of processes assigned to the grid along the x and y direction, respectively, as shown in Fig. 14. A layer of grid, named as guard grid or ghost grid, is set up at the junction of adjacent parallel regions to store the physical quantities received from the adjacent processes. The exchange of physical quantities on the guard grids is achieved through two MPI communication subroutine: MPI_SEND and MPI_RECV, as illustrated in Fig. 15.
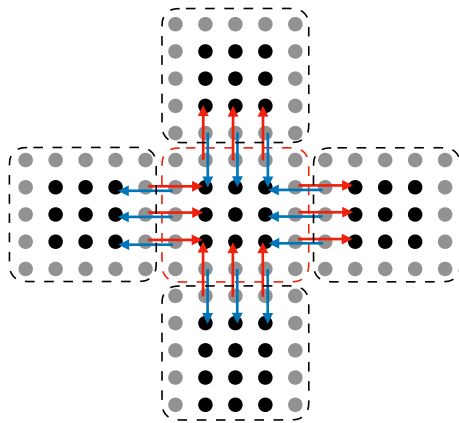
Fig. 15. MPI is utilized to update the guard grids. The dashed boxes represent parallel regions assigned to processors. The black and grey solid circles represent the grid points within the parallel region and guard points surrounding the parallel region, respectively. The red and blue arrow lines depict the communication that occurs between internal grid points and guard points across adjacent processors.

In the initialization, all pseudo-particles are placed within the parallel region and guard grids. When pseudo-particles are pushed out of the parallel region, they will be transferred to another parallel region by MPI communication. This communication can be realized between any two processors. Firstly, all communicating pseudo-particles are gathered into a linked list, then determining which processor's grid each pseudo-particle would fall in, and finally using the MPI communication subroutine to send the pseudo-particle to the corresponding processor. This procedure is illustrated in Fig. 16
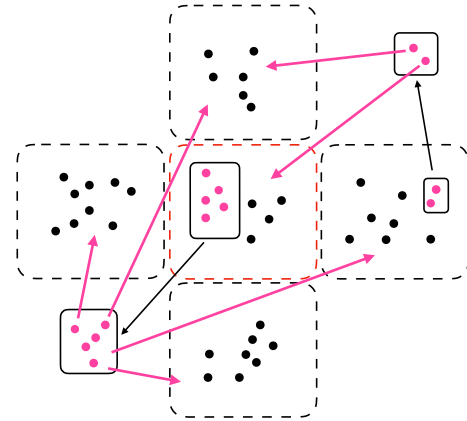

Fig. 16. MPI is utilized to facilitate the exchange of pseudo-particles. The magenta and black solid circles represent the pseudo-particles. The former indicates the pseudo-particles that require communication and the latter represent those that do not. The dashed boxes represent parallel regions. The black solid lines represent the link list containing all pseudo-particles to be communicated. The magenta and black arrow lines depict the communication between different processors.

[1] M. H. Johnson, B. A. Lippmann, Electromagnetic signals from nuclear explosions in outer space. Physical Review **119** 3, 827 (1960). doi: 10.1103/PhysRev.119.827

[2] W. Karzas, R. Latter, Electromagnetic radiation from a nuclear explosion in space. Physical Review **126** 6, 1919 (1962). doi: 10.1103/PhysRev.126.1919

[3] M. S. Smith, R. T. Santoro, Initial effects of nuclear weapon x-radiation on the LAMPSHADE orbital debris satellite shield. Report, (Oak Ridge National Lab.(ORNL), Oak Ridge, TN (United States), 1989). doi: 10.2172/5549195

[4] K. Zhang, Constitutive relationship of anisotropic composites and its application in a FEM simulation of the dynamic response within the X- ray radiation in 3D condition. Dissertation, (Graduate School of National University of Defense Technology, 2018) (in Chinese)

[5] S. Glasstone and P. J. Dolan, *The effects of nuclear weapons*. (US Department of Defense, Washington DC, 1977)

[6] N. J. Rudie (eds.), *Principles and techniques of radiation hardening*. (Western Periodicals Company, North Hollywood, 1976)

[7] Office of the Deputy Assistant Secretary of Defense for Nuclear Matters (ODASD(NM)), *Nuclear Matters Handbook*. (2020)

[8] H. Wang, Y-C. Lai, J-J. Zhong et al., Correction of distorted X-ray absorption spectra collected with capillary sample cell. Nuclear Science and Techniques **34** 7, 106 (2023) doi: 10.1007/s41365-023-01253-9

[9] R. W. Langley, Analytical relationships for estimating the effects of x-rays on materials. Report, (Huntington Beach, California: McDonnell Douglas Astronautics Company, 1974)

[10] R. Q. Zhang, J. F. Tan, Blowoff impulse on the cylindrical shell caused by x-ray energy flux. Acta Aerodynamica Sinica **119** 2, 178, (1989) (in Chinese)

[11] T. L. Cost, Dynamic Response of Missile Structures to Impulsive Loads Caused by Nuclear Effects Blowoff. Report, (Northport, AL, USA: Athena Engineering Company, 1976)

[12] R. J. Lawrence, The equivalence of simple models for radiation-induced impulse. In *Shock Compression of Condensed Matter–1991*, (Elsevier, Amsterdam, 1992) pp. 785 – 788

[13] J. L. Remo, M. D. Furnish, R. J. Lawrence, Plasma-driven Z-pinch X-ray loading and momentum coupling in meteorite and planetary materials. Journal of Plasma Physics **97** 2, 121 (2013). doi: 10.1017/S0022377812000712

[14] J. L. Remo, R. J. Lawrence, S. B. Jacobsen et al., High energy density soft x-ray momen- tum coupling to comet analogs for neo mitigation. Acta Astronautica **129**, 384 (2016). doi: 10.1016/j.actaastro.2016.09.02

[15] L. Seaman and D. R. Curran, Sri puff 8 computer program for one-dimensional stress wave propagation. SRI Report PYU-6802, (1978)

[16] E. S. Hertel, R. L. Bell, M. G. Elrick, Cth: A software family for multi-dimensional shock physics analysis. In *Shock Waves@ Marseille I*, (Springer, Berlin, Heidelberg, 1995) pp.

377 – 382. doi: 10.1007/978-3-642-78829-1_61

[17] Y. D. Murray et al., Users manual for ls-dyna concrete material model 159. Report, (United States: Federal Highway Administration, Office of Research, 2007)

[18] Group Abaqus, Abaqus 6.11. Mannual, (USA: Dassault Systemes Simulia Corporation, 2011)

[19] N. Zhou, D. J. Qiao, *Materials dynamics under pulse beam radiation*. (National Defense Industry Press, Beijing, China, 2002) pp 13-21 (in Chinese)

[20] D. J. Qiao, *Thermodynamic Effect and Reinforcing Technology under Pulse X-ray Radiation*. (National Defense Industry Press, Beijing, China, 2012) (in Chinese)

[21] D. Wang, Y. Gao, W. Chen et al., Equivalent analysis of thermo-dynamic blow-off impulse under x-ray irradiation. Applied Sciences **11** 19, 8853 (2012) doi: 10.3390/app11198853

[22] D. Wang, K, Zhang, W. H. Tang, Numerical Simulation of Thermal Shock Waves Induced by Pulsed X-ray in C/PF Materials. Journal of Physics: Conference Series **1865**, 022066 (2021) (IOP Publishing) doi: 10.1088/1742-6596/1865/2/022066

[23] S-C. Huang, H. Zhang, K. Bai et al., Monte Carlo study of the neutron ambient dose equivalent at the heavy ion medical machine in Wuwei. Nuclear Science and Techniques **33** 9, 119 (2022) doi: 10.1007/s41365-022-01093-z

[24] D-H. ShangGuan, W-H. Yan, J-X. Wei et al., Sample size adaptive strategy for time-dependent Monte Carlo particle transport simulation. Nuclear Science and Techniques **34** 4, 58 (2023) doi: 10.1007/s41365-023-01202-6

[25] M. W. Evans, F. H. Harlow, E. Bromberg, The particle-in-cell method for hydrodynamic calculations. Report, (Los Alamos Scientific Laboratory Los Alamos, 1957)

[26] F. H. Harlow, The particle-in-cell method for numerical solution of problems in fluid dynamics. Report, (Los Alamos National Lab.(LANL), Los Alamos, NM (United States), 1962)

[27] J. M. Dawson, Particle simulation of plasmas. Reviews of modern physics **55** 2, 403 (1983) doi: 10.1103/RevModPhys.55.403

[28] Y. N. Grigoryev, V. Vshivkov, *Numerical "particle-in-cell" methods: theory and applications*. (Walter de Gruyter, Zeist, Netherlands, 2012)

[29] N. A. Dyson, *X-rays in Atomic and Nuclear Physics*. (Cambridge University Press, London, 1990)

[30] E. Güneisen, Theorie des festen Zustandes einatomiger Elemente. Annalen der Physik **344** 12,257 (1912) doi: 10.1002/andp.19123441202 (in German)

[31] S. Faik, A. Tauschwitz, I. Iosilevskiy, The equation of state package FEOS for high energy density matter. Computer Physics Communications **227**, 117 (2018) doi: 10.1016/j.cpc.2018.01.008

[32] R. More, K. Warren, D. Young et al., A new quotidian equation of state (qeos) for hot dense matter. Physics of fluids **31** 10, 3059 (1988) doi: 10.1063/1.866963

[33] G. Zhao, R. Q, Zhang, W. H, Tang, Blowoff impulse on material due to pulsed x-ray radiation. Explosion and Shock Waves **16** 3, 260 (1996) (in Chinese)

[34] A. Nishiguchi and T. Yabe, Second-order fluid particle scheme. Journal of Computational Physics **52** 2, 390 (1983) doi: 10.1016/0021-9991(83)90037-2

[35] W. Gropp, E. Lusk, A. Skjellum, *Using MPI: portable parallel programming with the message-passing interface*. (MIT press, United States, 1999)

[36] S. Agostinelli, J. Allison, K. a. Amako et al., Geant4—a simulation toolkit. Nuclear instruments and methods in physics research section A: Accelerators, Spectrometers, Detectors and Associated Equipment **506** 3 250 (2003) doi: 10.1016/S0168-9002(03)01368-8

[37] J. Allison, K. Amako, J. Apostolakis et al., Geant4 developments and applications. IEEE Transactions on nuclear science **53** 1 270 (2006) doi: 10.1109/TNS.2006.869826

[38] J. Allison, K. Amako, J. Apostolakis et al., Recent developments in geant4. Nuclear instruments and methods in physics research section A: Accelerators, Spectrometers, Detectors and Associated Equipment **835** 186 (2016) doi: 10.1016/j.nima.2016.06.125

[39] J-L. Chen, S-J. Yun, T-K Dong et al., Studies of the radiation environment on the Mars surface using the Geant4 toolkit. Nuclear Science and Techniques **33** 1, 11 (2022) doi: 10.1007/s41365-022-00987-2

[40] W. Thomson, XLVI. hydrokinetic solutions and observations. The London, Edinburgh, and Dublin Philosophical Magazine and Journal of Science **42** 281, 362 (1871) (Published online 2009) doi: 10.1080/14786447108640585

[41] Helmholtz, XLIII. On discontinuous movements of fluids. The London, Edinburgh, and Dublin Philosophical Magazine and Journal of Science **36** 244, 337 (1868) (Published online 2009) doi: 10.1080/14786446808640073

[42] F. H. Ludlam, Characteristics of billow clouds and their relation to clear-air turbulence. Quarterly Journal of the Royal Meteorological Society **93** 398, 419 (1967) doi: 10.1002/qj.497093398033

[43] G. Bodo, S. Massaglia, A. Ferrari et al., Kelvin-helmholtz instability of hydrodynamic supersonic jets. Astronomy and Astrophysics **283** 2, 655 (1994)

[44] B. A. Remington, R. P. Drake, D. D. Ryutov, Experimental astrophysics with high power lasers and z pinches. Reviews of Modern Physics **78** 3, 755 (2006) doi: 10.1103/RevModPhys.78.755

[45] K. B. Antypas, A. C. Calder, A. Dubey et al., in *Parallel Computational Fluid Dynamics – Theory and Applications*. (Elsevier, Oxford, 2006)

[46] L-F. Wang, W-H. Ye, Z-F. Fan, et al., Kelvin-Helmholtz instability in compressible fluids. Acta Physica Sinica **59** 9, 6381 (2009) (in Chinese)

[47] J. She, Research on the Thermal-dynamic Response of Multi-thin-layer Structure Materials Irradiated by X-ray. Dissertation, (Graduate School of National University of Defense Technology, 2009) (in Chinese)

[48] C-X. Peng, H-M. Tan, P. Lin et al., Experimental studies of blowoff impulse in materials irradiated by pulsed soft X-ray. High Power Laser and Particle Beams **15** 1, 89 (2003) (in Chinese)

[49] G. M. Zhang, R. Q. Zhang, J. B. Chen, Two-dimensional Dynamic Calculation of X-ray Thermal Shock Wave in Cylindrical Shell. Journal of National University of Defense Technology **17** 2, 105 (1995) (in Chinese)